

1 **AnisoVeg: Anisotropy and Nadir-normalized MODIS MAIAC datasets for satellite**
2 **vegetation studies in South America**

3 Ricardo Dalagnol^{1,2,3,*}, Lênio Soares Galvão³, Fabien Hubert Wagner^{1,2}, Yhasmin Mendes
4 Moura^{4,5}, Nathan Gonçalves⁶, Yujie Wang^{7,8}, Alexei Lyapustin⁷, Yan Yang¹, Sassan Saatchi^{1,2},
5 Luiz Eduardo Oliveira Cruz Aragão^{3,9}

6 1 Center for Tropical Research, Institute of the Environment and Sustainability, University of
7 California, Los Angeles, Los Angeles, CA 90095, USA.

8 2 NASA-Jet Propulsion Laboratory, California Institute of Technology, Pasadena, CA 91109,
9 USA.

10 3 Earth Observation and Geoinformatics Division, National Institute for Space Research-INPE,
11 São José dos Campos, SP, 12227-010, Brazil.

12 4 Institute of Geography and Geoecology, Karlsruhe Institute of Technology, Karlsruhe,
13 Germany.

14 5 Centre for Landscape and Climate Research, School of Geography, Geology, and the
15 Environment, University of Leicester, Leicester, UK.

16 6 Michigan State University, Department of Forestry, College of Agriculture & Natural
17 Resources, East Lansing, MI, USA.

18 7 NASA Goddard Space Flight Center, Greenbelt, MD, United States.

19 8 Joint Center for Earth Systems Technology, University of Maryland Baltimore County, 1000
20 Hilltop Circle, Baltimore, MD.

21 9 Geography, College of Life and Environmental Sciences, University of Exeter, Exeter EX44RJ,
22 UK.

23

24 * Corresponding author. E-mail: ricds@hotmail.com.

25

26 **This document includes:** main manuscript, figures and tables.

27 Abstract

28 The AnisoVeg product consists of monthly 1-km composites of anisotropy (ANI) and nadir-normalized (NAD) surface reflectance layers obtained from the Moderate Resolution Imaging Spectroradiometer (MODIS) sensor over the entire South America. The satellite data were pre-processed using the Multi-Angle Implementation Atmospheric Correction (MAIAC). The AnisoVeg product spans 22 years of observations (2000 to 2021) and includes the reflectance of MODIS bands 1 to 8 and two vegetation indices (VIs): Normalized Difference Vegetation Index (NDVI) and Enhanced Vegetation Index (EVI). While the NAD layers reduce the data variability added by bidirectional effects on the reflectance and VI time series, the unique ANI layers allow the use of this multi-angular data variability as a source of information for vegetation studies. The AnisoVeg product has been generated using daily MODIS MAIAC data from both Terra and Aqua satellites, normalized for a fixed solar zenith angle ($SZA = 45^\circ$), modelled for three sensor view directions (nadir, forward, and backward scattering), and aggregated to monthly composites. The anisotropy was calculated by the subtraction of modelled backward and forward scattering surface reflectance. The release of the ANI data for open usage is novel, as well as the NAD data at an advance processing level. We demonstrate the use of such data for vegetation studies using three types of forests in eastern Amazon with distinct gradients of vegetation structure and aboveground biomass (AGB). The gradient of AGB was positively associated with ANI, while NAD values were related to different canopy structural characteristics. This was further illustrated by the strong and significant relationship between EVI_{ANI} and forest height observations from the Global Ecosystem Dynamics Investigation (GEDI) LiDAR sensor considering a simple linear model ($R^2 = 0.55$). Overall, the time series of the AnisoVeg product (NAD and ANI) provide distinct information for various applications aiming at understanding vegetation structure, dynamics, and disturbance patterns. All data, processing codes and results are made publicly available to enable research and the extension of AnisoVeg products for other regions outside the South America. The code can be found at <https://doi.org/10.5281/zenodo.6561351> (Dalagnol and Wagner, 2022), EVI_{ANI} and EVI_{NAD} can be found as assets in the Google Earth Engine (GEE) (described in the data availability section), and the full dataset is available at the open repository <<https://doi.org/10.5281/zenodo.3878879>> (Dalagnol et al., 2022).

56 **Key-words:** AnisoVeg, South America, vegetation structure, forest monitoring, MODIS.

58 1. Introduction

59 The anisotropy is defined as the departure from Lambertian scattering (isotropic), caused by the physical structure of media through which photons pass. ~~The anisotropy is defined by the directional dependence of observations on mechanical or physical properties of surfaces.~~ Because most land covers are not Lambertian (isotropic), the surface reflectance measured by satellite sensors varies with the view zenith angle (VZA), view direction (backward or forward scattering), and solar zenith angle (SZA) (Galvão et al., 2011). This is especially valid for images acquired over vegetated surfaces by large field-of-view (FOV) instruments such as the Moderate Resolution Imaging Spectroradiometer (MODIS) (Bhandari et al., 2011). MODIS has a wide swath scanning $\pm 55^\circ$ from nadir on board the Terra and Aqua satellites. For example, a reflected signal coming from the backward scattering direction of MODIS under a large VZA and close-to-zero relative azimuth angle (RAA) between the satellite and sun (sun behind the platform) is generally higher than that coming from the nadir ($VZA = 0^\circ$) or forward scattering direction (platform facing the sun at $RAA = 180^\circ$). Moreover, the SZA also varies seasonally and across geographical locations, affecting the amounts of shadows in the surfaces observed by satellites (Galvão et al., 2013). Such view-illumination effects are dependent on the land cover types and their magnitude relates to differences in biophysical properties of the vegetation (Galvão et al.,

2004; Sims et al., 2011; Foody & Curran, 1994). Therefore, the vegetation anisotropy can be seen antagonistically as sources of noise and biophysical information in the time-series analysis of vegetation indices (VIs) calculated from MODIS. As a source of noise, one may consider that the reflected signal toward the large FOV satellite sensors varies with distinct view-illumination geometries of data acquisition over the same surface. As a source of information, one may highlight that the anisotropy is land-cover type dependent, showing spectral variations that may be associated, for instance, with changes in vegetation structure across different forests.

To reduce the bidirectional effects as a source of noise, a nadir-normalized dataset can be created. We can normalize the surface reflectance of the MODIS bands to a specific set of VZA and SZA using the bidirectional reflectance distribution function (BRDF), represented by a model such as the Ross-Thick Li-Sparse (RTLS) (Wanner et al., 1995). To ensure confidence in the data analysis, we can also use the Multi-Angle Implementation Atmospheric Correction (MAIAC) for atmospheric correction. MAIAC is a new generation of cloud screening and atmospheric correction algorithm that uses an adaptive time series analysis and processing of groups of pixels to derive atmospheric aerosol concentration, cloud mask and surface reflectance without typical empirical assumptions (Lyapustin et al., 2011, 2012). By mitigating atmospheric interference and advancing the accuracy of surface reflectance over tropical vegetation by a factor of 3 to 10, MAIAC offers substantial improvement over conventional products such as the MOD09 (Hilker et al., 2012). Because of the better data quality retrieval, MAIAC is also an alternative to the MCD43A4 16-day Nadir Bidirectional Reflectance Distribution Function (BRDF)-Adjusted Reflectance (NBAR) product due to the less variable seasonal signal (3 to 10 times) over evergreen forests resultant from reduced effects of sun-view geometry. While the MCD43A4 NBAR product offers view-illumination correction, using the MAIAC products one can also correct for solar illumination effects at the same time. It offers substantial improvement over conventional algorithms by mitigating atmospheric interference and advancing the accuracy of surface reflectance over tropical vegetation by a factor of 3 to 10 (Hilker et al., 2012). Due to the improvements in cloud detection, aerosol retrieval and atmospheric correction, the MAIAC algorithm provides from 4 to 25% more high-quality retrievals than the traditional MOD09 product, with the largest estimate being observed for tropical regions (Lyapustin et al., 2021). Studies have used MODIS MAIAC observations with nadir-normalized geometry to assess Amazonian forests' structure, functioning, and impacts of environmental and climate change (Hilker et al., 2014; Wagner et al., 2017; Anderson et al., 2018; Dalagnol et al., 2018; Fonseca et al., 2019; Bontempo et al., 2020; Gonçalves et al., 2020; Zhang et al., 2021). For instance, such products provided reliable time series of surface reflectance data that allowed to identify large-scale communities of bamboo species and their dynamics in the southwest Amazon (Dalagnol et al., 2018). Lastly, by improving the cloud screening and minimizing BRDF artifacts in comparison to uncorrected data, the MAIAC greatly contributed to the understanding of the long-standing debate in the Amazon over the possible existence of the green-up phenomenon observed during the dry season of each year or with severe droughts (Morton et al., 2014; Bi et al., 2015; Saleska et al., 2016; Wu et al., 2017). The existence of this phenomenon has implications on the comprehension of the resilience of tropical forests to climate change.

To use the bidirectional effects as a source of information, we generate an anisotropy dataset that is dependent on land-cover types and captures the variations of sunlit and shaded canopy components viewed by the sensors (Chen et al., 2003; Gao, 2003). The use of multi-angular information to obtain metrics of anisotropy and extract information on forest structure was suggested two decades ago (Gobron et al., 2002; Diner et al., 2005; Foody & Curran, 1994). One of the early experiments exploring the use of anisotropy to extract information about vegetation structure were conducted by calculating the ratio between backward and forward scattering data and generating the anisotropy index (ANIX) on studying short-stature grass-type vegetation (Sandmeier et al., 1998). The first experiments with such concept were conducted by calculating

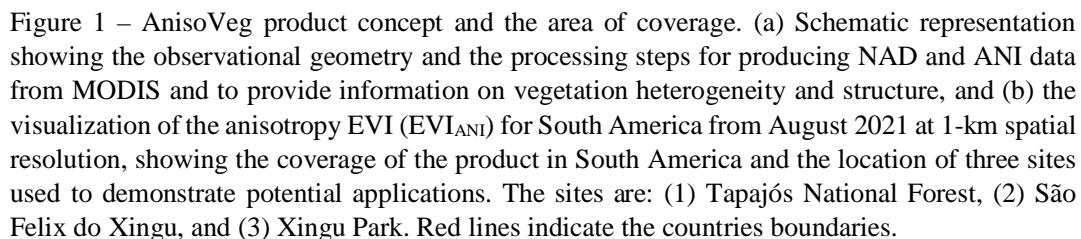
~~the ratio between backward and forward scattering data and generating the anisotropy index (ANIX) on studying short stature grass type vegetation (Sandmeier et al., 1998).~~ Other indices have been developed and validated afterwards (Schaaf et al., 2002; Lacaze et al., 2002; Chen et al., 2005; Pocewicz et al., 2007; Moura et al., 2015; Sharma et al., 2021). However, this remains an understudied topic with limited results reported in the literature, especially in tropical regions. For instance, observations from the Multi-angle Imaging Spectroradiometer (MISR)/Terra in the backward and forward scattering directions facilitated the discrimination of savanna physiognomies in Brazil (Liesenberg et al., 2007). MODIS MAIAC data from both directions were also used to calculate an anisotropic VI that explained part of the large-scale photosynthetic activity in the Amazon, where higher photosynthetic activity was associated to higher anisotropy values (Sousa et al., 2017). Moura et al. (2015) employed a more sophisticated approach based on scattering at backward and forward view directions using multi-temporal and multi-angular observations of MAIAC MODIS and BRDF modelling. The resultant metrics of anisotropy were further validated against field and airborne Light Detection And Ranging (LiDAR) observations, showing strong linear relationship with leaf area index (LAI) ($R^2 = 0.70-0.88$), canopy heterogeneity ($R^2 = 0.54$), and photosynthetic activity ($R^2 = 0.73-0.98$) (Moura et al., 2015; Moura et al., 2016; Hilker et al., 2017). Although showing great potential in vegetation studies, the aforementioned anisotropy metrics were never computed over larger areas of the world such as proposed in this study for South America.

The objective of this work is to present the AnisoVeg product, and how it can be used for vegetation studies. We use MODIS Collection 6 (C6) MAIAC (Lyapustin et al., 2018) monthly data (2000-2021) generated at 1-km spatial resolution for the entire South America with two different types of layers: (1) nadir-normalized (NAD) data for the surface reflectance of MODIS bands 1 to 8 and two VIs (NDVI and EVI); and (2) anisotropy data (ANI) calculated from the difference between backward and forwarding scattering estimates of bands 1 to 8 and VIs (Moura et al., 2015). The motivations for generating this product extend from developing applications of multi-angle observations for vegetation studies to producing analysis-ready and openly available datasets of anisotropy and nadir metrics for a larger community of users. The paper is organized in several sections to present the processing steps for generating the AnisoVeg products, a brief evaluation of data products over experimental areas, and finally an example of its potential application in vegetation studies.

2. Methodology to compute the AnisoVeg product

2.1. Daily MODIS MAIAC surface reflectance data over South America

Daily surface reflectance data were obtained from the MODIS product MCD19A1 v006 (collection 6) for the tiles covering South America (Figure 1). According to the MODIS traditional tiling system, these tiles ranged from 9-14 (horizontal) and 7-14 (vertical). The input data consisted in cross-calibrated surface reflectance from Terra and Aqua satellites on eight spectral bands (Table 1) with 1-km spatial resolution from 2000 to 2021 (Lyapustin & Wang, 2018; <http://dx.doi.org/10.5067/MODIS/MCD19A1.006>). This product provides surface reflectance data corrected for atmospheric effects by the MAIAC algorithm, and controlled for cloud-free and clear-to-moderately turbid conditions with Aerosol Optical Depth (AOD) at 0.47 μm below 1.5 (Lyapustin et al., 2018). The MAIAC algorithm uses a time series approach for improved cloud filtering amongst other filters such as surface reflectance change in order to provide the most accurate surface reflectance estimates. The raw data were obtained from the NASA's Level-1 and Atmosphere Archive and Distribution System (LAADS) Distributed Active Archive Center (DAAC) available at <https://ladsweb.modaps.eosdis.nasa.gov/archive/allData/6/MCD19A1/>.



Band number	Band name	Wavelength (nm)
1	Red	620–670
2	NIR-1	841–876
3	Blue-1	459–479
4	Green	545–565
5	NIR-2	1230–1250
6	SWIR-1	1628–1652
7	SWIR-2	2105–2155
8	Blue-2	405–420

The AnisoVeg product consists of two main types of data spanning from 2000 to 2021 in monthly composites at 1-km spatial resolution: (a) the nadir-normalized (NAD) data; and (b) the anisotropy (ANI) data. Each data type has 10 layers corresponding to the MODIS bands 1 to 8, and two VIs (NDVI and EVI). Additionally, the product provides auxiliary layers of backward scattering and forward scattering, including part of the bands (description on section 5). The

AnisoVeg product consists of two types of data spanning from 2000 to 2021 in monthly composites at 1 km spatial resolution: (a) the nadir normalized (NAD) data; and (b) the anisotropy (ANI) data. Each data type has 10 layers corresponding to the MODIS bands 1 to 8, and two VIs (NDVI and EVI).

2.2.1. The nadir-normalized (NAD) data

In order to minimize the differences in sun-sensor geometry between the MODIS scenes and generate the NAD dataset, the daily surface reflectance data were normalized to a fixed 45° SZA and to nadir observation (VZA = 0°) using the BRDF and the Ross-Thick Li-Sparse (RTLS) model (Wanner et al., 1995; Lucht and Lewis, 2000). Parameters of the RTLS BRDF model are part of the MAIAC product suite (MCD19A3 product) reported every 8 days. The MAIAC algorithm detects significant land cover changes (e.g. fire, deforestation) within the 8-day period and does not use those observations for the BRDF inversion (Lyapustin et al., 2018). A minimum of three observations in the eight-day window was required to accurately model the signal. The closest RTLS parameters in time were used to normalize the daily data. The normalized Bidirectional Reflectance Factor (BRF_n) for the NAD surface reflectance (SZA = 45°, VZA = 0°, RAA = 0°) was calculated using Eq. 1 (Lyapustin et al., 2018):

$$BRF_n = BRF \times \frac{k^L + F_{0V} \times k^V + F_{0G} \times k^G}{k^L + F_V \times k^V + F_G \times k^G} \quad (1)$$

where k^L , k^V , and k^G are the BRDF isotropic, volumetric, and geometric-optical kernel weights, respectively; F_{0V} and F_{0G} are the BRDF kernel values for the given geometry listed in Table 2; and F_V and F_G are the kernel values of the RTLS model for the specific MODIS observation, respectively (Lyapustin et al., 2018). F_V and F_G values are available at 5-km cells and were resampled to 1-km using the nearest neighbors' method to match the spatial resolution of the spectral bands. This resampling step does not create spatial artifacts in the data because the geometry changes slowly over time (Lyapustin et al., 2018).

Table 2 – View-angle normalizations and corresponding BRDF kernel values.

View-angle	<u>Solar Zenith Angle (SZA, °)</u>	<u>View Zenith Angle (VZA, °)</u>	<u>Relative Azimuth Angle (RAA, °)</u>	F_{0V}	F_{0G}
Nadir	45	0	0	-0.04578	- 1.10003
Backward scattering	45	35	180	0.22930469	0.017440045
Forward scattering	45	35	0	-0.12029795	-1.6218740

We aggregated normalized daily data into monthly composites by keeping the median values for each pixel. During the temporal aggregation, we also calculated the per-pixel number of samples (or observations) for each monthly composite, which can be used as auxiliary data to filter pixels with low number of observations (less reliable estimates of surface reflectance). The tiles were mosaicked for the entire South America and then re-projected from the original sinusoidal projection to the geographic coordinates system (datum WGS-84, EPSG 4326). The output spatial resolution corresponded to 0.009107388 degrees, which is approximately equivalent to 1 km in projected coordinates.

We also calculated two traditional vegetation indices: NDVI (Rouse et al., 1973) (Eq. 2) and EVI (Huete et al., 2002) (Eq. 3).

$$NDVI = \frac{\rho_{NIR} - \rho_{Red}}{\rho_{NIR} + \rho_{Red}} \quad (2)$$

$$EVI = 2.5 \times \frac{\rho_{NIR} - \rho_{Red}}{\rho_{NIR} + (6 \times \rho_{Red} - 7.5 \times \rho_{Blue}) + 1} \quad (3)$$

where ρ is the surface reflectance of a MODIS band, ρ_{NIR} is the NIR reflectance (band 2), ρ_{Red} is the red reflectance (band 1), and ρ_{Blue} is the blue reflectance (band 3). The constants in Eq. 3 (6, 7.5, 1, and 2.5) represent: the aerosol coefficient adjustment of the atmosphere for the red and blue bands; the adjustment factor for the soil; and the gain factor, respectively (Huete et al., 2002).

2.2.2. The anisotropy (ANI) data

For the ANI data, the daily surface reflectance data was first normalized to two viewing-angles at the backward (SZA = 45°, VZA = 35°, RAA = 180°) and forward (SZA = 45°, VZA = 35°, RAA = 0°) scattering using Eq. 1 and values from Table 2. The VZA was set to near hotspot (VZA = 35°) instead of the actual hotspot (VZA = 45°) to keep VZA closer to the actual range of MODIS observations across the South America and minimize errors coming from extrapolation of the BRDF (Moura et al., 2015). ~~To minimize potential errors of BRDF extrapolation, the VZA was set to 35° instead of the hotspot (45°), because 35° is a very common VZA in the empirical data distribution of the South America, and thus providing better estimates of the anisotropy (Moura et al., 2015).~~ The standard deviation for this modelling was thoroughly investigated in a previous study and determined as 10% of the observed variation in anisotropy (Moura et al., 2015). Further, we aggregated the backward and forward scattering data temporally into monthly composites following the same procedures as before for the NAD data. We then calculated the NDVI and EVI for each of the view-angle normalizations. Finally, we obtained the difference between backward and forward scattering estimates for each of the eight MODIS bands, as well as for the NDVI and EVI, effectively generating the ANI layers (Eq. 4; Moura et al., 2015):

$$ANI_i = Backward_i - Forward_i \quad (4)$$

where i is the spectral band or VI selected in the calculation.

2.3. Algorithm and computation

All data processing was done in R v4.0.2 (R Core Team, 2016) and the code is available at GitHub (https://github.com/ricds/maiac_processing) (Dalagnol & Wagner, 2022). Besides processing the AnisoVeg product from the daily MAIAC MODIS data, the code can also generate 16-day or 8-day temporal composites, mosaics, and VIs. Although we focused on South America when developing AnisoVeg, the code can readily be adapted to process data for other parts of the world and generate corresponding NAD and ANI layers. Below, we provide the computer specification for anyone who wishes to process the data independently.

For the presented dataset, the computation was performed under a HP Z840 Workstation with Intel Xeon CPU E5-2640 v3 (2.60Ghz, 32 cores), and 64 ~~Gb~~ GB (gigabytes) RAM memory. The daily MODIS data for the whole South America from 2000 to 2021 accounted for 6.69 ~~Tb~~ TB

(terabytes). Processing monthly composites is computationally intensive due to loading all daily data for each month at once for a given tile. Thus, the main bottlenecks are RAM memory and hard drive writing speed. For the workstation with 64 ~~Gb~~-GB memory, the usage of 10 cores running in parallel processing was the optimal choice. The average processing time of each monthly composite for one tile was 6 minutes. Therefore, it took 26.2 hours to process the 262 composites (March 2000 to December 2021) for each tile. Since we had 31 tiles covering the South America, the total amount of time to process one view-normalization was approximately a month (33.8 days). Consequently, the total time spent in computation was 101.5 days for processing the three view-normalizations (nadir, backward, and forward scattering) and generating the NAD and ANI layers. Processing can also be done with less potent computers with a minimum of 16 ~~Gb~~-GB RAM memory and 4 processing cores.

2.4. Time series availability and uncertainty

The monthly compositing process returned a time series dataset over all of South America with an average of 242 ± 35 out of a maximum of 262 composites (period between March 2000 and December 2021) for each pixel with some data missing due to lack of high-quality observations (Figure 2). Only 34.3% of the available pixels have the full time series (262 composites). The Amazon region shows a lower mean number of samples in the time series with an average of 231 ± 29 composites, which can be seen in Figure 2. This lower number of samples is due to the innate high cloud cover (Durieux et al., 2003). It is important to note that the AnisoVeg product was strictly created to analyze land surface and does not cover water bodies. Moreover, the period between March 2000 and June 2002 has higher amounts of missing data because it preceded the launch of the Aqua satellite. When data from both satellites (Terra and Aqua) were combined to create the product after 2002, we had a much better pixel level data availability to produce dense time series. Although we have a dense time series across the Amazon rainforests (Figure 2a), the mean number of daily observations within a month for this region is relatively lower than that observed in more dry and seasonal regions of South America (Figure 2b). Thus, we suggest using the number of samples layer as a proxy for uncertainty on the retrieval of monthly composites to filter out pixels with low number of samples (e.g., less than three observations per composite). The lesser number of samples one pixel has, the higher the uncertainty in the data analysis. Although we use the median values to aggregate observations within months and mitigate potential land cover changes, stand-replacing changes may cause inaccurate anisotropy estimates for the given monthly estimates. Hence, we advise filtering data for land use and land cover changes before using them to obtain the most accurate anisotropy estimates.

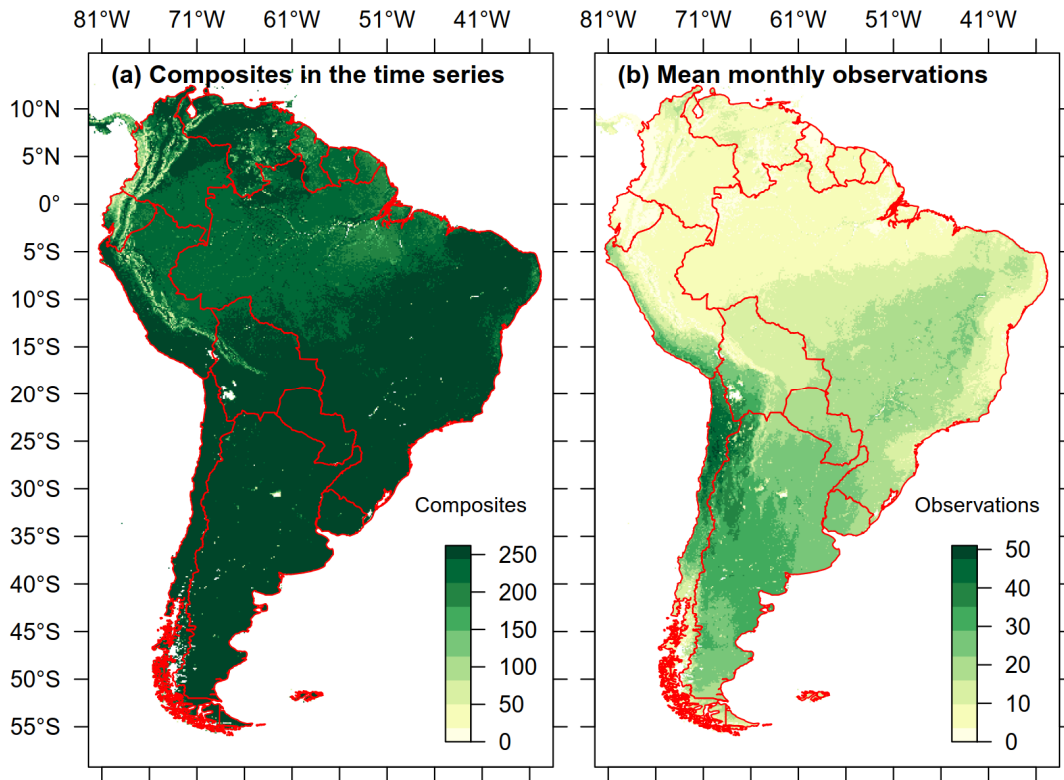


Figure 2 – AnisoVeg time series availability and uncertainty over South America. (a) The number of composites in the time series representing pixel availability. The maximum number of composites in the time series is 262 for the period between March 2000 and December 2021. (b) Mean number of daily observations within a month used to create the monthly composites as a proxy for uncertainty. The maximum daily observations in a composite are 60 (twice a day every day for a month).

3. Spatial and temporal distribution of NAD and ANI data across the Amazon forests

We selected three experimental areas at the Brazilian Amazon rainforests to show the spatial and temporal distribution of NAD and ANI data (rectangles in Figure 1). To demonstrate the spatial and temporal distribution of NAD and ANI data over the Brazilian Amazon rainforests, we selected three experimental areas (rectangles in Figure 1). These areas show old-growth rainforests with distinct canopy structure and aboveground biomass (AGB) stocks. The AGB increases from semideciduous forests at the Xingu Park ($190 \pm 19 \text{ Mg ha}^{-1}$) and open ombrophilous forests with lianas at the São Felix do Xingu ($241 \pm 31 \text{ Mg ha}^{-1}$) to dense ombrophilous forests at the Tapajós National Forest ($288 \pm 38 \text{ Mg ha}^{-1}$), as estimated by the ESA/CCI AGB map from 2017 (Santoro & Cartus, 2021). These are large-scale AGB estimates and may underestimate the true AGB at higher values such as in the Tapajós site. These three sites are also expected to show different phenological dynamics because their selected pixels cover distinct phenoregions in the study reported by Xu et al. (2015).

When compared to the nadir-normalized EVI (EVI_{NAD}) images (Figures 3a, b, c), the anisotropy EVI (EVI_{ANI}) data showed different spatial patterns across sites (Figures 3d, e, f). While the forests over the three sites showed approximately similar EVI_{NAD} values ($\text{EVI}_{\text{NAD}} \approx 0.50$) (Figures 3a,b,c), they showed more variability in EVI_{ANI} between the Xingu Park ($\text{EVI}_{\text{ANI}} > 0.20$), São Felix do Xingu ($\text{EVI}_{\text{ANI}} > 0.24$), and Tapajós ($\text{EVI}_{\text{ANI}} > 0.27$) sites (Figures 3d,e,f). This increase

in EVI_{ANI} between sites goes into the same direction of the AGB gradient observed from the Xingu Park to the Tapajós National Forest. This result may indicate different forest canopy structures that were not captured in the EVI_{NAD} observations, but were captured by the EVI_{ANI} . Overall, the EVI_{ANI} is high over forests (0.20 to 0.30) and low over pastures and crops (less than 0.10). This means large anisotropy between the reflected energy in backward and forward scattering MODIS directions due to the structural complexity of forest canopies. The association between anisotropy and forest canopy structure has been previously shown for the same region in a previous work (Moura et al., 2016).

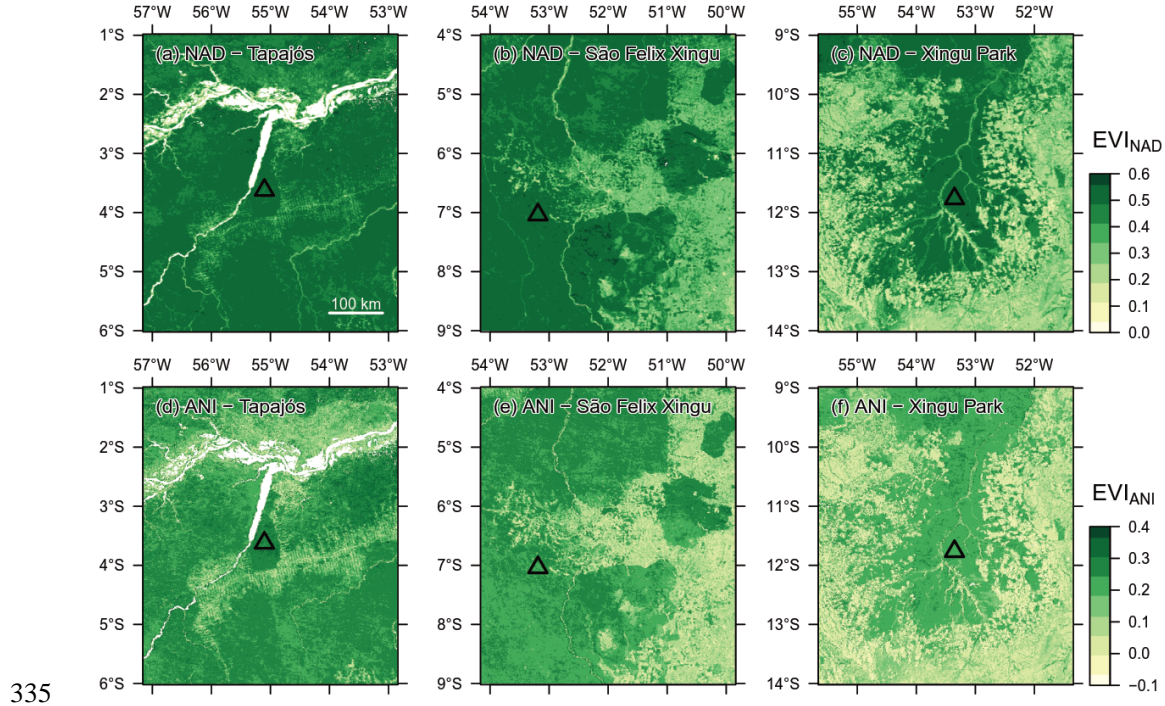


Figure 3 – The spatial distribution in August 2020 (dry season) of the nadir-normalized Enhanced Vegetation Index (EVI_{NAD}) is shown in (a), (b), and (c) for the Tapajós National Forest, São Felix do Xingu and Xingu Park, respectively. Corresponding results for the anisotropy EVI (EVI_{ANI}) are shown in (d), (e), and (f), respectively. The triangles plotted over (a, b, and c) indicate the sites used to obtain the profiles of Figure 4.

From the comparison of different sites (triangles in Figure 3a), we observed that the mean EVI_{NAD} signal over the time period did not vary much between the selected forests, while the EVI_{ANI} varied greatly (Figure 4): Tapajós (mean EVI_{NAD} = 0.49, mean EVI_{ANI} = 0.27), São Felix do Xingu (mean EVI_{NAD} = 0.51, mean EVI_{ANI} = 0.24), and Xingu Park (mean EVI_{NAD} = 0.51, mean EVI_{ANI} = 0.22). Moreover, EVI_{NAD} and EVI_{ANI} values were moderately positively correlated at Tapajós (r = +0.37), weakly correlated at São Felix do Xingu (r = +0.06), and moderately negatively correlated at the Xingu Park (r = -0.28). The EVI_{NAD} and EVI_{ANI} are seasonal variability and phase correlation changes from site to site, suggesting that different canopy dynamics processes are likely being captured by the two metrics at the three sites. Understanding exactly what those effects mean for these forests is beyond the scope of this paper. However, it indicates open venues for studying forest functioning using these products. For example, previous studies have shown that EVI_{NAD} metrics captured different compositions of leaf ages in the canopies of the central Amazon (Gonçalves et al., 2020).

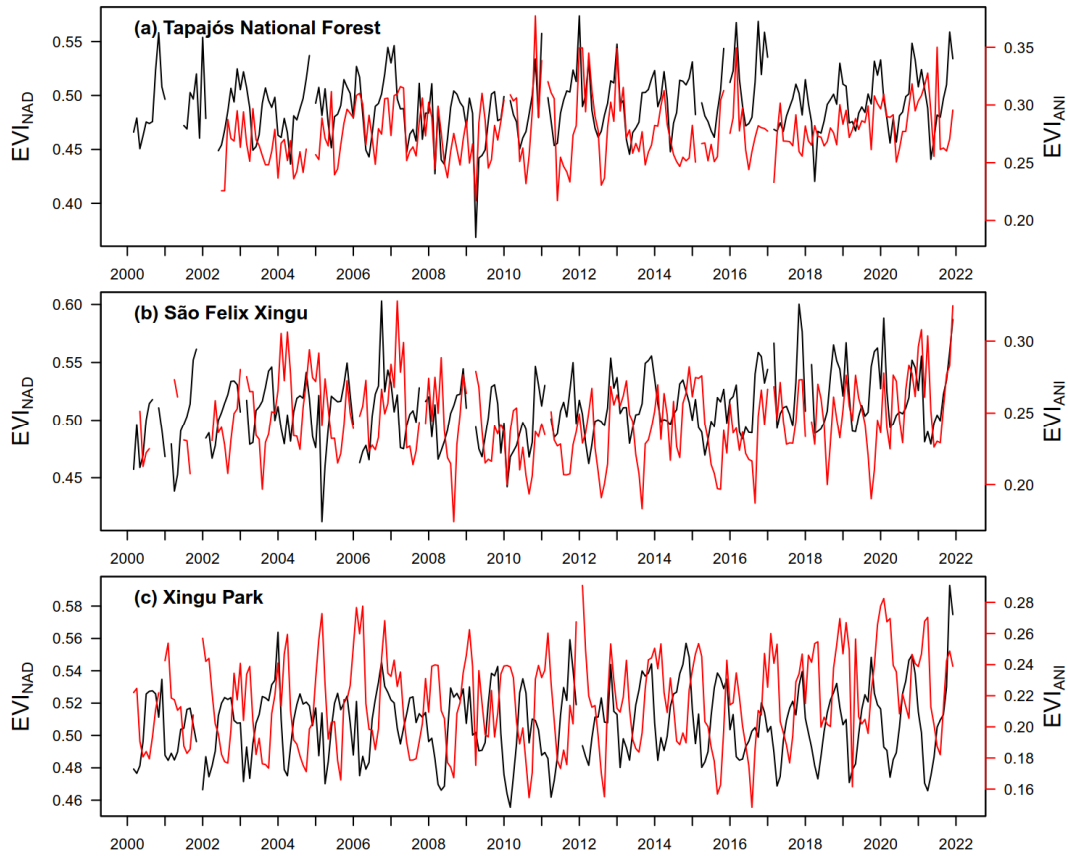


Figure 4 – Time series of AnisoVeg’s MODIS Enhanced Vegetation Index (EVI) from 2000 to 2021 for old-growth forests of the (a) Tapajós National Forest; (b) São Felix do Xingu; (c) Xingu Park. The black line indicates the nadir-normalized signal (NAD layer), while the red line represents the EVI anisotropy (ANI layer). The profiles are the mean value of 3 x 3 pixels whose locations are indicated by triangles in Figure 3.

To demonstrate the potential of AnisoVeg for large-scale forest structure inference, we compared the NAD and ANI data against forest height measurements from the Global Ecosystem Dynamics Investigation (GEDI) LiDAR sensor. We found that EVI_{ANI} was able to explain up to 55% of height variability of Amazon forests according to a simple linear relationship ($R^2 = 0.55$, $p < 0.01$, Figure 5). This is a very strong predicting power for a single variable, considering a simple linear model, especially for satellite passive optical data which are often underrated for forest structure estimates in comparison to Synthetic Aperture Radar (SAR) data. EVI_{NAD} was significantly but weakly associated to height variability ($R^2 = 0.16$, $p < 0.01$), reinforcing the increase in explanation power owed to the anisotropy metrics built from multi-angle observations. The height data was derived from the GEDI LiDAR sensor aboard the International Space Station. They were obtained more specifically from the product GEDI L2A elevation and height metrics data version 2 (footprint size 25 m), acquired from April 2019 to October 2020 (available dates at the time of download). GEDI data were downloaded from Earth Data cloud service system (<https://earthdata.nasa.gov>). We selected the Relative Height metric at 98th percentile (RH98), which represents the top canopy height. The selected RH98 metric was averaged over each 1-km grid cell, and filtered using a threshold of greater than or equal to 50 shots per km² to have a high confidence of reliable height estimation representing the 1-km mean. The AnisoVeg data used for this comparison were based on the same time period as GEDI, and filtered for EVI_{NAD} larger than 0.35 to exclude non-forested areas. While we only showed the plot for the strongest EVI_{ANI} :GEDI relationship in June 2019 (Figure 5), the other months also showed significant ($p < 0.01$) and

strong relationships with R^2 ranging from 0.36 to 0.55 (mean $R^2 = 0.46$). Future studies should explore relationships using ANI from different months and other indices, alone or in combination with each other, to further understand their significance ~~on~~for explaining forest structure. This is important to determine how the anisotropy data can contribute for aboveground biomass and carbon estimates in conjunction with other sources of data such as those from SAR sensors.

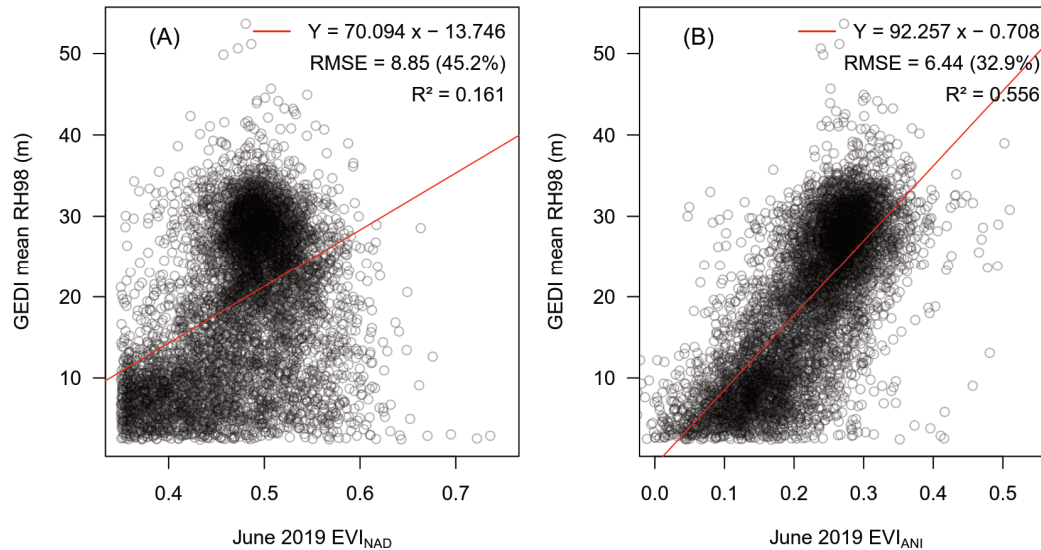


Figure 5 – Relationship between forest height (GEDI mean RH98) and two AnisoVeg layers obtained in June 2019 over the Amazon: (a) EVI_{NAD} and (b) EVI_{ANI} . The RH98 metric ~~consists~~ ~~inis~~ the relative height at the 98th percentile, which represents the top of canopy height. 7,000 random matching pixels were used in this analysis (1% of 700,000 total matching pixels available), resulting from the filtering of both GEDI and AnisoVeg data. The red line indicates the fitted line by a simple linear model.

Terrain illumination is a factor of spectral variability, which can affect EVI_{NAD} determination and its relationship with biophysical attributes of vegetation, as shown by previous literature (Huang et al., 2010; Chen and Cao, 2012). Even at 1-km spatial resolution, EVI_{ANI} results of Figures 3, 4 and 5 can be affected to some extent by terrain illumination effects observed locally at some sites. For instance, topographic effects on EVI_{ANI} occurred probably at the São Felix do Xingu site where topographic roughness, observed in SRTM data (results not shown), was coincident with increased EVI_{ANI} values in Figure 3E. Furthermore, even in relatively flat terrains, variations in topographic aspect (surface orientation to Sun) can affect the EVI variability in MODIS data because of the different amounts of energy reflected in the NIR towards the sensor by inclined surfaces in the forward and backscattering view directions. Such effects have been observed in southern Brazil with MODIS at 250-m spatial resolution and increased in magnitude at higher spatial resolution data obtained by other sensors (Galvão et al., 2016). Therefore, it may prove useful to include topographic variables in modelling exercises to offset these effects.

In a prospective analysis, we also explored the behavior of the two EVI AnisoVeg metrics over the Amazonian phenoregions mapped by Xu et al. (2015). The EVI_{NAD} and EVI_{ANI} monthly means over different phenoregions highlighted the strong heterogeneity of the Amazonian forests (Figure 6). For instance, the profiles showed strong differences between both metrics from January to September in a phenoregion with well-defined dry and wet seasons (phenoregion one in Figure 6a at the Xingu Park). Large differences between EVI_{NAD} and EVI_{ANI} were also observed in some phenoregions without a very long dry season in ~~the~~ northwest Amazon (phenoregion five in Figure 6e). On the other hand, EVI_{NAD} and EVI_{ANI} showed temporal decoupling in phenoregion

three located at central-east Amazon (Figure 6c). Overall, while the seasonality of EVI_{NAD} has been investigated by many studies in the past, the seasonality of EVI_{ANI} is something to be further explored with the support of auxiliary data (e.g., airborne LiDAR and field campaigns). This is important to better understand the differences in seasonal patterns between both AnisoVeg metrics.

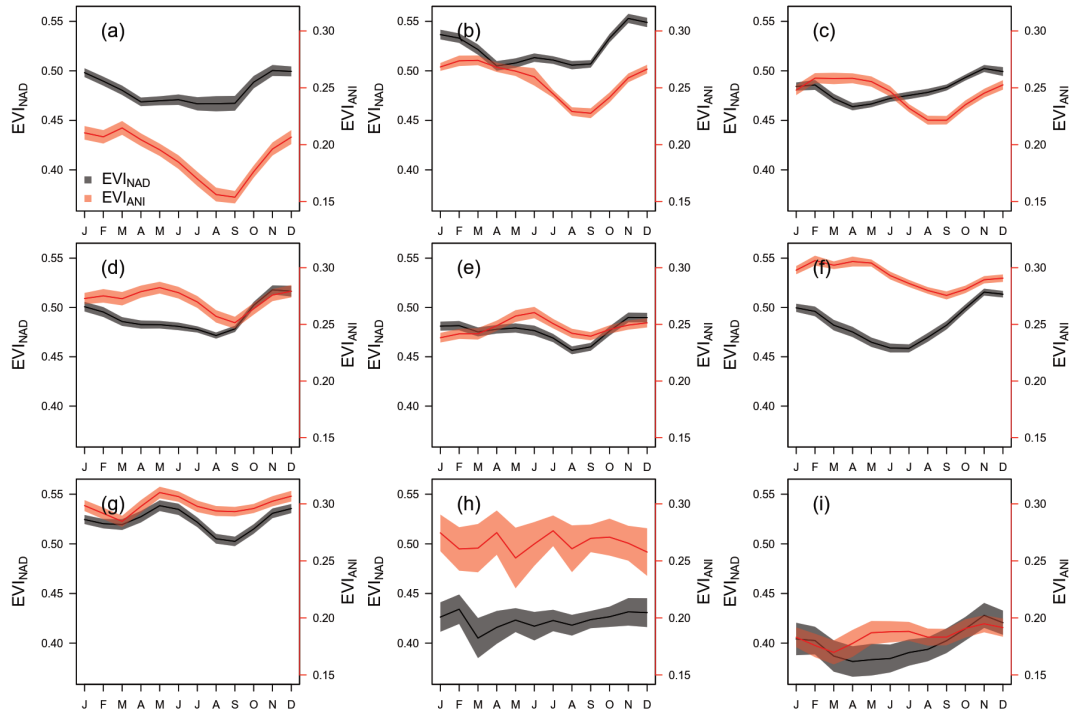


Figure 6 – Monthly means of EVI_{NAD} (black) and EVI_{ANI} (red) for nine phenoregions mapped by Xu et al. (2015) in the Amazon. The phenoregions are shown in increasing order from 1 to 9 in corresponding panels (a) to (i). They represent forests with similar seasonality and landscape structure. Solid line and shaded area represent the mean and 95% confidence interval around the mean. The values were extracted from 20 years of data (from 2001 to 2021) for 100 random coordinates within each region, and extracted from 3 x 3 windows of pixels.

4. Prospective use of the dataset

The NAD layers from the AnisoVeg product have been used in previous studies to explore: the climate drivers of the Amazon forest greening (Wagner et al., 2017); the large-scale Amazon forest sensitivity to drought (Anderson et al., 2018); the structure and dominance of bamboo species in southwest Amazon (Dalagnol et al., 2018); the productivity in a flooded forest in eastern Amazon (Fonseca et al., 2019); the productivity and relationship with Sun-Induced Fluorescence over the Brazilian Caatinga biome (Bontempo et al., 2020); the relationships with leaf-age demography in central Amazon (Gonçalves et al., 2020); and the relationships with fire disturbance and SAR-based Vegetation Optical Depth in southern Amazon (Zhang et al., 2021).

The ANI layers from the AnisoVeg product have been mainly used to characterize Amazon forest structure properties (Moura et al., 2015; 2016). These layers now open new venues of investigation on vegetation, including (but not limited to): the characterization of biophysical attributes of forests, including their seasonality and trends; the assessment of changes in vegetation structure due to natural disturbances or degradation (logging, fire, edge effects); and the evaluation of forest health and productivity (greenness and browning). We expect that this

dataset contributes to upscaling studies over large areas of key forest properties such as the AGB and canopy roughness (Foody & Curran, 1994; Saatchi et al., 2008). This information is required for dynamic vegetation models to accurately represent the carbon cycle. This dataset is not limited to study Amazonian forests and can be used to explore other biomes of South America such as the Atlantic Forest, savannas (Cerrado), Caatinga, Chaco, Pantanal, and Pampas. Such studies could improve our understanding of large-scale vegetation functioning, carbon storage, and cycling. Ultimately, they can contribute to refine global ecosystem models, and to obtain accurate estimates of carbon cycle in response to climate and environmental change. [Furthermore, auxiliary backward and forward scattering data are also available with the dataset. Beyond the use of the provided ANI layers, this effectively allows the computation of several other multi-angular anisotropy indices from the literature \(Table 3\). The advantage or disadvantage of one specific anisotropy index rather than others is not established in the literature given the range of vegetation applications and the lack of available datasets up to date. We calculated and provided only ANI due to its demonstrated relationships with Amazonian forests structure and functioning \(Moura et al., 2015; Moura et al., 2016; Hilker et al., 2017\). However, we expect other indices, including ratios and normalized differences between the backward and forward scattering components, offer additional possibilities for tropical vegetation studies which should be explored in future studies.](#) ~~Furthermore, auxiliary backward and forward scattering data are also available with the dataset. Beyond the use of the provided ANI layers, this effectively allows the computation of several other multi-angular anisotropy indices from the literature (Table 3), offering the possibility to investigate their use for tropical vegetation studies.~~

Table 3 – Examples of other multi-angular anisotropy indices that can be further calculated using layers of the AnisoVeg product. Lambda represents the selected spectral band or vegetation index. N, [HB](#), and [DF](#) represent nadir-view normalization, [hot-spot](#) (backward scattering), and [dark-spot](#) (forward scattering) estimates, respectively.

Anisotropy Indices	Formula	Reference
Anisotropy index (ANIX)	$\frac{\lambda_{HB}}{\lambda_{DF}}$	Sandmeier et al. (1998)
Nadir BRDF-adjusted NDVI (NDVI_{ISO})	$\frac{NIR_N - RED_N}{NIR_N + RED_N}$	Schaaf et al. (2002)
Hot-spot dark-spot index (HDS_{RED})	$\frac{RED_{HB} - RED_{DF}}{RED_{DF}}$	Lacaze et al. (2002)
Normalized difference between hot-spot and dark-spot index (NDHD_{NIR})	$\frac{NIR_{HB} - NIR_{DF}}{NIR_{HB} + NIR_{DF}}$	Chen et al. (2005)
Hot-spot dark-spot NDVI (NDVI_{HD})	$\frac{NIR_{HB} - RED_{DF}}{NIR_{HB} + RED_{DF}}$	Pocewicz et al. (2007)
Hot-spot-incorporated NDVI (NDVI_{HS})	$NDVI_N \times (1 - RED_{HB})$	Pocewicz et al. (2007)
Anisotropy difference (ANI)*	$\lambda_{HB} - \lambda_{DF}$	Moura et al. (2015)
Vegetation Structure Index (VSI)	$\frac{NDVI_{DF} - NDVI_{HB}}{1 - NIR_{DF}}$	Sharma et al. (2021)

*ANI is included in the AnisoVeg product. Source: Adapted from Sharma et al. (2021).

5. Code and data availability

All code is available at GitHub (https://github.com/ricds/maiac_processing) (Dalagnol & Wagner, 2022). The full dataset can be found at the official AnisoVeg repository at Zenodo

(<https://doi.org/10.5281/zenodo.3878879>) (Dalagnol et al., 2022). The dataset was organized in compressed files (“.zip” format) sub-divided by years (currently 2000-2021) and layers (bands 1-8, NDVI, and EVI) for both nadir-normalization (code = NAD) and anisotropy (code = ANI). The number of samples layers (code = NO_SAMPLES) are also provided. Inside each compressed file there will be 12 image files (“.tif” format), one per month, except for the year 2000 which starts in March. The storage size for the whole dataset is 162.6 GB. The data have a scale factor of 10,000 to reduce file storage size. Thus, to obtain surface reflectance values of bands or correct range of values for indices, you should divide the layers by 10,000. The exception is the number of samples, which already shows the correct range of values from 0 to 60 observations. The dataset is planned to be updated on a yearly-basis. Auxiliary data that allow the calculation of other anisotropy metrics (listed in Table 3) are included in two separate Zenodo repositories for backward (<https://doi.org/10.5281/zenodo.6040300>) (Dalagnol, 2022a) and forward scattering (<https://doi.org/10.5281/zenodo.6048785>) (Dalagnol, 2022b), including the selected layers Red, NIR, NDVI and EVI. The EVI_{ANI} and EVI_{NAD} layers were also uploaded to the GEE platform using the *geeup* tool v0.5.3 (Roy, 2022). They can be accessed through the GEE ImageCollection assets “projects/anisoveg/assets/evi_anisotropy” and “projects/anisoveg/assets/evi_nadir”, found at <https://code.earthengine.google.com/?asset=projects/anisoveg/assets/evi_anisotropy> and <https://code.earthengine.google.com/?asset=projects/anisoveg/assets/evi_nadir>.

Author contribution

R.D. and Y.M. conceived the presented idea. R.D. designed the methodology with contributions from Y.M. on the anisotropy method. R.D. conducted formal analysis and investigation with contributions from L.G., F.W., N.G., and S.S. Y.W. and A.L. provided the original MODIS (MAIAC) data and support for processing it. Y.Y. and S.S. provided the processed GEDI height data and support to analyze it. R.D. and F.W. developed the code to process the MODIS (MAIAC) data into the products. R.D. conducted data curation of the products. L.A. supervised the project. R.D. wrote the original draft with support from L.G., F.W. and Y.M. All authors read, reviewed and approved the final version of the manuscript.

Acknowledgements

R.D. was supported by Sao Paulo Research Foundation (FAPESP) grants 2015/22987-7 and 2019/21662-8. F.W. was supported by FAPESP grant 2015/50484-0. Part of this work was carried out at the Jet Propulsion Laboratory, California Institute of Technology, under a contract with the National Aeronautics and Space Administration (NASA). The funders had no role in the study design, data collection and analysis, including the decision to publish or prepare the manuscript. We thank the MODIS MAIAC team from NASA for providing the freely available MODIS (MAIAC) daily dataset. [The authors thank the comments from Bruce Nelson and three anonymous reviewers who helped improve this manuscript.](#)

Conflict of Interest

The authors have declared no conflict of interest.

References

516 Anderson, L. O., Ribeiro Neto, G., Cunha, A. P., Fonseca, M. G., Mendes de Moura, Y.,
517 Dalagnol, R., Wagner, F. H., & Aragão, L. (2018). Vulnerability of Amazonian forests to
518 repeated droughts. *Philosophical Transactions of the Royal Society B: Biological Sciences*,
519 373(1760), 20170411. <https://doi.org/10.1098/rstb.2017.0411>

520 Bhandari, S., Phinn, S., & Gill, T. (2011). Assessing viewing and illumination geometry effects
521 on the MODIS vegetation index (MOD13Q1) time series: implications for monitoring
522 phenology and disturbances in forest communities in Queensland, Australia. *International*
523 *Journal of Remote Sensing*, 32(22), 7513–7538.
524 <https://doi.org/10.1080/01431161.2010.524675>

525 Bi, J., Knyazikhin, Y., Choi, S., Park, T., Barichivich, J., Ciais, P., Fu, R., Ganguly, S., Hall, F.,
526 Hilker, T., Huete, A., Jones, M., Kimball, J., Lyapustin, A. I., Mörtus, M., Nemani, R. R.,
527 Piao, S., Poulter, B., Saleska, S. R., ... Myneni, R. B. (2015). Sunlight mediated
528 seasonality in canopy structure and photosynthetic activity of Amazonian rainforests.
529 *Environmental Research Letters*, 10(6). <https://doi.org/10.1088/1748-9326/10/6/064014>

530 Bontempo, E., Dalagnol, R., Ponzoni, F., & Valeriano, D. (2020). Adjustments to aid the
531 interpretation of drought responses at the caatinga of Northeast Brazil. *Remote Sensing*,
532 12(19), 1–29. <https://doi.org/10.3390/rs12193264>

533 Chen, J. M., Menges, C. H., & Leblanc, S. G. (2005). Global mapping of foliage clumping
534 index using multi-angular satellite data. *Remote Sensing of Environment*, 97(4), 447–457.
535 <https://doi.org/10.1016/j.rse.2005.05.003>

536 Chen, J. M., Liu, J., Leblanc, S. G., Lacaze, R., & Roujean, J. L. (2003). Multi-angular optical
537 remote sensing for assessing vegetation structure and carbon absorption. *Remote Sensing*
538 *of Environment*, 84(4), 516–525. [https://doi.org/10.1016/S0034-4257\(02\)00150-5](https://doi.org/10.1016/S0034-4257(02)00150-5)

539 [Chen, W., & Cao, C. \(2012\). Topographic correction-based retrieval of leaf area index in](#)
540 [mountain areas. *Journal of Mountain Science*, 9\(2\), 166–174.](#)
541 <https://doi.org/10.1007/s11629-012-2248-2>

542 Dalagnol, R., Wagner, F. H., Galvão, L. S., Nelson, B. W., & Aragão, L. (2018). Life cycle of
543 bamboo in the southwestern Amazon and its relation to fire events. *Biogeosciences*,
544 15(20), 6087–6104. <https://doi.org/10.5194/bg-15-6087-2018>

545 Dalagnol, Ricardo; Galvão, Lênio Soares; Wagner, Fabien Hubert; Moura, Yhasmin Mendes;
546 Gonçalves, Nathan; Wang, Yujie; Lyapustin, Alexei; Yang, Yan; Saatchi, Sassan; Aragão,
547 Luiz Eduardo Oliveira e Cruz. (2022). "AnisoVeg: Anisotropy and Nadir-normalized
548 MODIS MAIAC datasets for satellite vegetation studies in South America". (Version v1)
549 [Data set]. Zenodo. <https://doi.org/10.5281/zenodo.3878879>

550 Dalagnol, Ricardo. (2022a). Back scattering data of AnisoVeg: Anisotropy and Nadir-
551 normalized MODIS MAIAC datasets for satellite vegetation studies in South America
552 [Data set]. Zenodo. <https://doi.org/10.5281/zenodo.6040300>

553 Dalagnol, Ricardo. (2022b). Forward scattering data of AnisoVeg: Anisotropy and Nadir-
554 normalized MODIS MAIAC datasets for satellite vegetation studies in South America
555 [Data set]. Zenodo. <https://doi.org/10.5281/zenodo.6048785>

556 Dalagnol, R., & Wagner, F. H. (2022). maiac_processing: Script and functions to process daily
557 MODIS MAIAC data to BRDF-corrected 16-day and monthly mosaic composites.
558 (Version 1.0) [Computer software]. Zenodo. <https://doi.org/10.5281/zenodo.6561351>

559 de Moura, Y. M., Hilker, T., Lyapustin, A. I., Galvão, L. S., dos Santos, J. R., Anderson, L. O.,
560 de Sousa, C. H. R., & Arai, E. (2015). Seasonality and drought effects of Amazonian
561 forests observed from multi-angle satellite data. *Remote Sensing of Environment*, 171,
562 278–290. <https://doi.org/10.1016/j.rse.2015.10.015>

563 de Sousa, C. H. R., Hilker, T., Waring, R., de Moura, Y. M., & Lyapustin, A. (2017). Progress
564 in remote sensing of photosynthetic activity over the amazon basin. *Remote Sensing*, 9(1),
565 1–23. <https://doi.org/10.3390/rs9010048>

566 Durieux, L., Toledo Machado, L. A., & Laurent, H. (2003). The impact of deforestation on
567 cloud cover over the Amazon arc of deforestation. *Remote Sensing of Environment*, 86(1),
568 132–140. [https://doi.org/10.1016/S0034-4257\(03\)00095-6](https://doi.org/10.1016/S0034-4257(03)00095-6)

569 Fonseca, L. D. M., Dalagnol, R., Malhi, Y., Rifai, S. W., Costa, G. B., Silva, T. S. F., Da Rocha,
570 H. R., Tavares, I. B., & Borma, L. S. (2019). Phenology and Seasonal Ecosystem
571 Productivity in an Amazonian Floodplain Forest. *Remote Sensing*, 11(13), 1530.
572 <https://doi.org/10.3390/rs11131530>

573 Foody, G. M., & Curran, P. J. (1994). Estimation of Tropical Forest Extent and Regenerative
574 Stage Using Remotely Sensed Data. *Journal of Biogeography*, 21(3), 223.
575 <https://doi.org/10.2307/2845527>

576 Galvão, L. S., Breunig, F. M., Santos, J. R. dos, & Moura, Y. M. de. (2013). View-illumination
577 effects on hyperspectral vegetation indices in the Amazonian tropical forest. *International*
578 *Journal of Applied Earth Observation and Geoinformation*, 21(1), 291–300.
579 <https://doi.org/10.1016/j.jag.2012.07.005>

580 Galvão, L. S., dos Santos, J. R., Roberts, D. A., Breunig, F. M., Toomey, M., & de Moura, Y.
581 M. (2011). On intra-annual EVI variability in the dry season of tropical forest: A case
582 study with MODIS and hyperspectral data. *Remote Sensing of Environment*, 115(9), 2350–
583 2359. <https://doi.org/10.1016/j.rse.2011.04.035>

584 Gao, F., Schaaf, C. B., Strahler, A. H., Jin, Y., & Li, X. (2003). Detecting vegetation structure
585 using a kernel-based BRDF model. *Remote Sensing of Environment*, 86(2), 198–205.
586 [https://doi.org/10.1016/S0034-4257\(03\)00100-7](https://doi.org/10.1016/S0034-4257(03)00100-7)

587 [Galvão, L. S., Breunig, F. M., Teles, T. S., Gaida, W., & Balbinot, R. \(2016\). Investigation of](#)
588 [terrain illumination effects on vegetation indices and VI-derived phenological metrics in](#)
589 [subtropical deciduous forests. *GIScience and Remote Sensing*, 53\(3\), 360–381.](#)
590 <https://doi.org/10.1080/15481603.2015.1134140>

591 Gatti, L. V., Basso, L. S., Miller, J. B., Gloor, M., Gatti Domingues, L., Cassol, H. L. G.,
592 Tejada, G., Aragão, L. E. O. C., Nobre, C., Peters, W., Marani, L., Arai, E., Sanches, A.
593 H., Corrêa, S. M., Anderson, L., Von Randow, C., Correia, C. S. C., Crispim, S. P., &
594 Neves, R. A. L. (2021). Amazonia as a carbon source linked to deforestation and climate
595 change. *Nature*, 595(7867), 388–393. <https://doi.org/10.1038/s41586-021-03629-6>

596 Gonçalves, N. B., Lopes, A. P., Dalagnol, R., Wu, J., Pinho, D. M., & Nelson, B. W. (2020).
597 Both near-surface and satellite remote sensing confirm drought legacy effect on tropical
598 forest leaf phenology after 2015/2016 ENSO drought. *Remote Sensing of Environment*,
599 237(April 2019), 111489. <https://doi.org/10.1016/j.rse.2019.111489>

600 Hilker, T., Galvão, L. S., Aragão, L. E. O. C., de Moura, Y. M., do Amaral, C. H., Lyapustin, A.
601 I., Wu, J., Albert, L. P., Ferreira, M. J., Anderson, L. O., dos Santos, V. A. H. F.,

602 Prohaska, N., Tribuzy, E., Barbosa Ceron, J. V., Saleska, S. R., Wang, Y., de Carvalho
603 Gonçalves, J. F., de Oliveira Junior, R. C., Cardoso Rodrigues, J. V. F., & Garcia, M. N.
604 (2017). Vegetation chlorophyll estimates in the Amazon from multi-angle MODIS
605 observations and canopy reflectance model. *International Journal of Applied Earth*
606 *Observation and Geoinformation*, 58, 278–287. <https://doi.org/10.1016/j.jag.2017.01.014>

607 Hilker, T., Lyapustin, A. I., Tucker, C. J., Hall, F. G., Myneni, R. B., Wang, Y., Bi, J., De
608 Moura, Y. M., & Sellers, P. J. (2014). Vegetation dynamics and rainfall sensitivity of the
609 Amazon. *Proceedings of the National Academy of Sciences of the United States of*
610 *America*, 111(45), 16041–16046. <https://doi.org/10.1073/pnas.1404870111>

611 Hilker, T., Lyapustin, A. I., Tucker, C. J., Sellers, P. J., Hall, F. G., & Wang, Y. (2012). Remote
612 sensing of tropical ecosystems: Atmospheric correction and cloud masking matter. *Remote*
613 *Sensing of Environment*, 127, 370–384. <https://doi.org/10.1016/j.rse.2012.08.035>

614 Huete, A., Didan, K., Miura, T., Rodriguez, E. ., Gao, X., & Ferreira, L. . (2002). Overview of
615 the radiometric and biophysical performance of the MODIS vegetation indices. *Remote*
616 *Sensing of Environment*, 83(1–2), 195–213. [https://doi.org/10.1016/S0034-](https://doi.org/10.1016/S0034-4257(02)00096-2)
617 [4257\(02\)00096-2](https://doi.org/10.1016/S0034-4257(02)00096-2)

618 Lacaze, R., Chen, J. M., Roujean, J. L., & Leblanc, S. G. (2002). Retrieval of vegetation
619 clumping index using hot spot signatures measured by POLDER instrument. *Remote*
620 *Sensing of Environment*, 79(1), 84–95. [https://doi.org/10.1016/S0034-4257\(01\)00241-3](https://doi.org/10.1016/S0034-4257(01)00241-3)

621 Liesenberg, V., Galvão, L. S., & Ponzoni, F. J. (2007). Variations in reflectance with
622 seasonality and viewing geometry: Implications for classification of Brazilian savanna
623 physiognomies with MISR/Terra data. *Remote Sensing of Environment*, 107(1–2), 276–
624 286. <https://doi.org/10.1016/j.rse.2006.03.018>

625 Lucht, W., & Lewis, P. (2000). Theoretical noise sensitivity of BRDF and albedo retrieval from
626 the EOS-MODIS and MISR sensors with respect to angular sampling. *International*
627 *Journal of Remote Sensing*, 21(1), 81–98. <https://doi.org/10.1080/014311600211000>

628 Lyapustin, A. I., Wang, Y., Laszlo, I., Hilker, T., G.Hall, F., Sellers, P. J., Tucker, C. J., &
629 Korkin, S. V. (2012). Multi-angle implementation of atmospheric correction for MODIS
630 (MAIAC): 3. Atmospheric correction. *Remote Sensing of Environment*, 127, 385–393.
631 <https://doi.org/10.1016/j.rse.2012.09.002>

632 Lyapustin, A., Martonchik, J., Wang, Y., Laszlo, I., & Korkin, S. (2011). Multiangle
633 implementation of atmospheric correction (MAIAC): 1. Radiative transfer basis and look-
634 up tables. *Journal of Geophysical Research Atmospheres*, 116(3).
635 <https://doi.org/10.1029/2010JD014985>

636 Lyapustin, A., & Wang, Y. (2018). MCD19A1 MODIS/Terra+Aqua Land Surface BRDF Daily
637 L2G Global 500m, 1km and 5km SIN Grid V006 [Data set]. *NASA EOSDIS Land*
638 *Processes DAAC*. <https://doi.org/10.5067/MODIS/MCD19A1.006>

639 Lyapustin, A., Wang, Y., Korkin, S., & Huang, D. (2018). MODIS Collection 6 MAIAC
640 algorithm. *Atmospheric Measurement Techniques*, 11(10), 5741–5765.
641 <https://doi.org/10.5194/amt-11-5741-2018>

642 Lyapustin, A., Zhao, F., & Wang, Y. (2021). A Comparison of Multi-Angle Implementation of
643 Atmospheric Correction and MOD09 Daily Surface Reflectance Products From MODIS.

644 *Frontiers in Remote Sensing*, 2(December), 1–15.
645 <https://doi.org/10.3389/frsen.2021.712093>

646 Matricardi, E. A. T., Skole, D. L., Costa, O. B., Pedlowski, M. A., Samek, J. H., & Miguel, E. P.
647 (2020). Long-term forest degradation surpasses deforestation in the Brazilian Amazon.
648 *Science*, 369(6509), 1378–1382. <https://doi.org/10.1126/SCIENCE.ABB3021>

649 Morton, D. C., Nagol, J., Carabajal, C. C., Rosette, J., Palace, M., Cook, B. D., Vermote, E. F.,
650 Harding, D. J., & North, P. R. J. (2014). Amazon forests maintain consistent canopy
651 structure and greenness during the dry season. *Nature*, 506(7487), 221–224.
652 <https://doi.org/10.1038/nature13006>

653 Moura, Y. M. de, Hilker, T., Gonçalves, F. G., Galvão, L. S., dos Santos, J. R., Lyapustin, A.,
654 Maeda, E. E., & de Jesus Silva, C. V. (2016). Scaling estimates of vegetation structure in
655 Amazonian tropical forests using multi-angle MODIS observations. *International Journal*
656 *of Applied Earth Observation and Geoinformation*, 52(January), 580–590.
657 <https://doi.org/10.1016/j.jag.2016.07.017>

658 Pocewicz, A., Vierling, L. A., Lentile, L. B., & Smith, R. (2007). View angle effects on
659 relationships between MISR vegetation indices and leaf area index in a recently burned
660 ponderosa pine forest. *Remote Sensing of Environment*, 107(1–2), 322–333.
661 <https://doi.org/10.1016/j.rse.2006.06.019>

662 R Core Team. (2016). *R: A Language and Environment for Statistical Computing* (3.3.1; Vol. 1,
663 Issue C, p. 2016). R Foundation for Statistical Computing. <https://www.r-project.org/>

664 Samapriya Roy. (2022). samapriya/geeup: geeup: Simple CLI for Earth Engine Uploads (0.5.3).
665 Zenodo. <https://doi.org/10.5281/zenodo.5814026>

666 Rouse, J. W., Hass, R. H., Schell, J. A., & Deering, D. W. (1974). Monitoring Vegetation
667 Systems in the Great Plains with ERTS. *Third Earth Resources Technology Satellite-1*
668 *Symposium*, 1, 301–317.

669 Saleska, S. R., Wu, J., Guan, K., Araujo, A. C., Huete, A., Nobre, A. D., & Restrepo-Coupe, N.
670 (2016). Dry-season greening of Amazon forests. *Nature*, 531(7594), E4–E5.
671 <https://doi.org/10.1038/nature16457>

672 Samanta, A., Ganguly, S., Hashimoto, H., Devadiga, S., Vermote, E., Knyazikhin, Y., Nemani,
673 R. R., & Myneni, R. B. (2010). Amazon forests did not green-up during the 2005 drought.
674 *Geophysical Research Letters*, 37(5), 1–5. <https://doi.org/10.1029/2009GL042154>

675 Samanta, A., Knyazikhin, Y., Xu, L., Dickinson, R. E., Fu, R., Costa, M. H., Saatchi, S. S.,
676 Nemani, R. R., & Myneni, R. B. (2012). Seasonal changes in leaf area of Amazon forests
677 from leaf flushing and abscission. *Journal of Geophysical Research: Biogeosciences*,
678 117(1), 1–13. <https://doi.org/10.1029/2011JG001818>

679 Sandmeier, S., Müller, C., Hosgood, B., & Andreoli, G. (1998). Physical mechanisms in
680 hyperspectral BRDF data of grass and watercress. *Remote Sensing of Environment*, 66(2),
681 222–233. [https://doi.org/10.1016/S0034-4257\(98\)00060-1](https://doi.org/10.1016/S0034-4257(98)00060-1)

682 Santoro, M., & Cartus, O. (2021). *ESA Biomass Climate Change Initiative (Biomass_cci):*
683 *Global datasets of forest above-ground biomass for the years 2010, 2017 and 2018* (No.
684 2). Centre for Environmental Data Analysis.
685 <https://doi.org/http://dx.doi.org/10.5285/84403d09cef3485883158f4df2989b0c>

686 Schaaf, C. B., Gao, F., Strahler, A. H., Lucht, W., Li, X., Tsang, T., Strugnell, N. C., Zhang, X.,
687 Jin, Y., Muller, J., Lewis, P., Barnsley, M., Hobson, P., Disney, M., Roberts, G.,
688 Dunderdale, M., Doll, C., Robert, P., Hu, B., ... Roy, D. (2002). Schaaf et al 2002 First
689 operational BRDF, albedo nadir reflectance products from MODIS.pdf. *Remote Sensing of*
690 *Environment*, 83, 135–148.

691 Wagner, F. H., Hérault, B., Rossi, V., Hilker, T., Maeda, E. E., Sanchez, A., Lyapustin, A. I.,
692 Galvão, L. S., Wang, Y., & Aragão, L. E. O. C. (2017). Climate drivers of the Amazon
693 forest greening. *PLoS ONE*, 12(7), 1–15. <https://doi.org/10.1371/journal.pone.0180932>

694 Wanner, W., Li, X., & Strahler, a H. (1995). On the derivation of kernels for kernel-driven
695 models of bidirectional reflectance. *Journal of Geophysical Research*, 100(D10), 21077.
696 <https://doi.org/10.1029/95JD02371>

697 [Wei, H., Zhang, L., Furumi, S., Muramatsu, K., Daigo, M., & Li, P. \(2010\). Topographic effects](#)
698 [on estimating net primary productivity of green coniferous forest in complex terrain using](#)
699 [Landsat data: A case study of Yoshino Mountain, Japan. *International Journal of Remote*](#)
700 [*Sensing*, 31\(11\), 2941–2957. <https://doi.org/10.1080/01431160903140829>](#)

701 Wu, J., Kobayashi, H., Stark, S. C., Meng, R., Guan, K., Tran, N. N., Gao, S., Yang, W.,
702 Restrepo-Coupe, N., Miura, T., Oliveira, R. C., Rogers, A., Dye, D. G., Nelson, B. W.,
703 Serbin, S. P., Huete, A. R., & Saleska, S. R. (2018). Biological processes dominate
704 seasonality of remotely sensed canopy greenness in an Amazon evergreen forest. *New*
705 *Phytologist*, 217(4), 1507–1520. <https://doi.org/10.1111/nph.14939>

706 Xu, L., Saatchi, S. S., Yang, Y., Myneni, R. B., Frankenberg, C., Chowdhury, D., & Bi, J.
707 (2015). Satellite observation of tropical forest seasonality: Spatial patterns of carbon
708 exchange in Amazonia. *Environmental Research Letters*, 10(8).
709 <https://doi.org/10.1088/1748-9326/10/8/084005>

710 Zhang, H., Hagan, D. F. T., Dalagnol, R., & Liu, Y. (2021). Forest Canopy Changes in the
711 Southern Amazon during the 2019 Fire Season Based on Passive Microwave and Optical
712 Satellite Observations. *Remote Sensing*, 13(12), 2238. <https://doi.org/10.3390/rs13122238>